Supplementary Material for
Similarity between oxygen evolution in photosystem II and oxygen reduction in cytochrome *c* oxidase via proton coupled electron transfers. A unified view of the oxygenic life from four electron oxidation-reduction reactions

SI Historical developments of broken symmetry (BS) and post BS methods for chemical reactions

SI. 1 Molecular orbital models for chemical reactions

In this paper, theoretical and computational methods for transition-metal enzymes are not described in detail in the main text. In the supporting material, broken symmetry (BS) methods are mainly explained since they are now handy and practical for theoretical investigations of biological redox reactions involving one electron transfer (ET) processes. In this paper, BS methods [20] are mainly applied to elucidate similarity between the four-electron oxidation and reduction reactions, namely four time one ET processes, in PSII [1, 2] and C*c*O [3, 4]. Therefore, we summarized physical foundations of our theoretical methods employed for theoretical investigations of metalloenzymes in Fig. 1 in the main text.

In the supporting section, historical developments of BS methods are examined in relation to the concepts of orbital symmetry and broken symmetries. Orbital symmetry conservation rule by Woodward and Hoffmann [38, 39] was the guiding principle for theoretical investigation of chemical reactions in late 1960s and early 1970s. To this end, Hückel [40] and extended Hückel [41] methods have been used for elucidation of spatially symmetry-adapted molecular orbitals (MO). Since then, the Woodward-Hoffmann (WH) rule based on the Hückel MO (HMO) [40] and extended Hückel MO (EHMO) [41] has been applied for elucidation and predictions of various types of concerted reactions, where the closed-shell MO nature of chemical bonds is retained in a sharp contrast to the redox reactions in eq. (1). We can remember the famous message for the violation of the WH rule; *there are none* [39]. The concept of the orbital symmetry conservation is consistent with the fundamental theorem, so-called Noether's theorem [42] relating with the symmetry and conservation law revealed in the mathematical physics.

On the other hand, HMO and EHMO obtained by neglecting the electron repulsion effects are not sufficient for MO-theoretical descriptions of symmetry-forbidden diradical reactions by the WH rule because of lack of orbital bifurcation to reduce the electron repulsion effect and emergence of local spins [32]. In early 1970s, we searched appropriate MO-models including this repulsion effect explicitly for diradicals with the singlet and triplet spin states, and found that Hubbard [36], Kanamori [43] and Gutzwiller [44] already proposed effective model Hamiltonians involving the electron repulsion effects (U) with different spins in the singlet diradical. The Hubbard Hamiltonian for magnetic materials such as

manganese oxides (Mn_xO_y) was written in the second quantization notation including electron spin σ in the solid-state physics

$$H = \sum_{i,j,\sigma} -t_{ij}\left(C_{i,\sigma}^{+}C_{j,\sigma} + C_{j,\sigma}^{+}C_{i,\sigma}\right) + U\sum_i n_{i,\uparrow}\, n_{i,\downarrow} \quad \text{(s1)}$$

where $C_{i,\sigma}^{+}$ denotes the operator which creates an electron with σ = ↑, ↓ at site i, and t_{ij} is the transfer integral, and U denotes the on-site repulsion integral. The corresponding annihilation operator is $C_{i,\sigma}$, and the $n_{i,\sigma} = C_{i,\sigma}^{+}C_{i,\sigma}$ is the spin density operator for spin σ on the i-th site. These fermion operators obey the canonical anticommutation relations.

$$\left\{C_{i,\sigma}^{+}, C_{j,\tau}\right\} = \delta_{ij}\delta_{\sigma\tau},\ \left\{C_{i,\sigma}^{+}, C_{j,\tau}^{+}\right\} = \left\{C_{i,\sigma}, C_{j,\tau}\right\} = 0 \quad \text{(s2)}$$

The transfer integrals of the on-site (t_{ii}) and nearest sites (t_{ij}) are chemically referred to as the Coulomb integral ($-\alpha_{ii}$) and resonance integral (β_{ij}) in the HMO model. Therefore, the Hubbard model [36] in physics was referred to as the Hückel-Hubbard model in our chemistry papers [34].

Hubbard models [36] have been used for investigations of complex charge density wave (CCDW) and spin density wave (SDW) states in solid-state physics [22, 24]. SDW is responding for spin-polarized (SP) UHF in quantum chemistry [32]. In 1970s–1990s, radical reactions with active oxygens and oxyradical generated in photocatalytic reactions [52–55] were investigated by BS SP UHF methods [56–58] as touched in the main text. The SP BS method is still useful for MO-theoretical modeling of inorganic magnetic clusters embedded in protein matrix [45] as illustrated in Fig. 1. Thus, from our theoretical view [20, 45], the $CaMn_4O_5$ cluster in PSII is regarded as a strongly correlated electron system (SCEM) with several kinds of quantum freedom [35] as examined in sections II–IV in the main text.

SI.2 Instability of chemical bonds and HOMO-LUMO mixing

The Hückel-Hubbard model [34, 35] may be regarded as a simplified version of the Hartree-Fock (HF) independent particle model [46] that provides symmetry-adapted molecular orbitals (MO) used for MO-modeling of the concerted reactions of molecules. To this end, the spatial symmetries of the highest-occupied MO (HOMO) and the lowest unoccupied MO (LUMO) [47] play important roles for theoretical elucidation of the symmetry-allowed concerted reactions for which the HOMO-LUMO energy gap is sufficiently large to prevent the singlet and triplet instability revealed by the classic paper by Čížek and Paldus [23, 25] and Fukutome [24]. On the other hand, the HOMO-LUMO energy gap (Δε) becomes small for symmetry-forbidden diradical reactions, indicating the triplet instability of the HF MO solution

[23–25]

$$\Delta\varepsilon / U = \varepsilon_{\mathrm{LUMO}} - \varepsilon_{\mathrm{HOMO}} / U < 1 \tag{s3}$$

where the ε_X (X = HOMO, LUMO) denotes the orbital energy of X [32].

The instability condition indicates that the closed-shell bond is reorganized into the more stable spin-polarized (SP) bond given by the unrestricted (U) Hubbard [36] and Hartree-Fock (HF) [46] solutions. The resulting MOs at the UHF level of theory are indeed given by the HOMO-LUMO mixing by the restricted (R) HF (RHF) solution [32, 35]:

$$\psi_i^+ = \cos\theta\,\phi_i + \sin\theta\,\phi_i^* \tag{s4a}$$

$$\psi_i^- = \cos\theta\,\phi_i - \sin\theta\,\phi_i^* \tag{s4b}$$

where θ denotes the orbital mixing-parameter determined by UHF computations. Since HOMO, ϕ_i and LUMO, ϕ_i^*, by RHF are symmetry-adapted and usually belong to different spatial symmetries (P_{n}), UHF MOs, ψ_i^+ and ψ_i^-, obtained by the HOMO-LUMO mixing are often spatially symmetry-broken as shown in Fig. 2. The "broken symmetry (BS)" orbitals are responding to local electrons with up- or down-spins (↑ or ↓) which are often represented with the dot （•↑ or ↓•） in radical reactions [32].

SI.3 Radical reactivity revealed by broken-symmetry (BS) orbitals of several BS methods

In early 1970s, the ab-initio UHF computations were hardly possible for large systems such as transition-metal clusters. Slater and his collaborators have developed the Hartree-Fock-Slater (HFS) model [48] where molecular exchange integral (Fock term) in the HF model has been approximated with the density functional by the Thomas-Fermi-Dirac model [49]. The HFS model was applied to elucidate the nature of the 3d metal-metal bonds that exhibit the temperature-dependent paramagnetism [50]. The unrestricted HFS (UHFS) model is regarded as a precursor model for the unrestricted Kohn-Sham (UKS) density functional theory (DFT) [49] model and many other unrestricted DFT (UDFT) models. The UHFS, UDFT, and hybrid UHF-UDFT (HDFT) [64, 65] models are also regarded as independent particle models based on the single Slater determinant. Nowadays, HDFT models have been effectively used for theoretical investigations of metalloenzymes [20, 21]. The HOMO-LUMO mixing procedure in eq. (9) [32] has been useful enough for construction of the broken-symmetry (BS) orbitals based on these theoretical models. Therefore, several methods mentioned above are often regarded as BS methods in general. The BS methods have first elucidated the oxy-radical character of the high-valent transition-metal oxo bonds [59–62] as illustrated in Fig. 2 in the main text.

SI.4 Reduction of bond order by orbital symmetry breaking

MO model has been used for theoretical investigation of the nature of the chemical bond [51]. Over past decades, several chemical indices have been employed to investigate the nature of chemical bonds of open-shell systems expressed by eq. (s4). For example, the orbital overlap T_i between BS MOs obtained by the HOMO-LUMO mixing in eq. (s4) is defined as [32, 35]

$$T_i = \langle \psi_i^+ | \psi_i^- \rangle = \cos 2\theta \tag{s5}$$

Therefore, T_i becomes 1.0 in the case of the closed-shell (restricted) case; $\psi_i^+ = \psi_i^- = \phi_i$, whereas T_i is 0.0 for the complete mixing case ($\theta = \pi/4$): complete SP split pair in accord with the order parameter in the phase transition. In order to express the decrease of chemical bonding via orbital symmetry breaking, the Coulson's (first order) effective bond order [51] is defined by [32]

$$b_i = \frac{n_i - n_i^*}{2} = \frac{(1+\cos 2\theta) - (1-\cos 2\theta)}{2} = \cos 2\theta = T_i \tag{s6}$$

where n_i and n_i^* denote the occupation numbers of the bonding (HOMO) and antibonding (LUMO) orbitals, respectively, and they are expressed by using the orbital overlap; $n_i = 1 + T_i$ and $n_i^* = 1 - T_i$ [32]. The effective bond order (b) is nothing but the orbital overlap between BS MOs under the BS approximations.

SI.5 Homolytic di- and poly-radicals: *n*-electrons and *n*-orbitals [*n*e, *n*o]

In early 1970s, elucidation of scope and reliability of the BS method for chemical reactions was an important theoretical problem. Analytical solutions for [n electrons, n orbitals] references (n = 2–4) have been obtained to elucidate functional behaviors of the BS solutions [33–35]. To this end, the Hubbard model [36] of the two-center two-electron system [2e, 2o] for diradicals was first solved to understand the essential role of the electron repulsion (U) in chemical bonding [35]. To this end, the covalent bonding parameter (x) is defined to express the magnitude of the chemical bonding.

$$x = {}^{t}/_{U} = -{}^{\beta}/_{U} \tag{s7a}$$

The normalized total energy of the restricted Hartree-Fock (RHF) solution (E_{RHF}) [46] for the closed-shell bond of the [2e, 2o] system is given by [35]

$$E_{\mathrm{RHF}} = \frac{E(RHF)-2\alpha}{U} = -2x + \frac{1}{2} \quad \text{(s8a)}$$

where α denotes the afore-mentioned Coulomb integral for the HMO model. On the other hand, the SP UHF solution emerges in the weak covalent bonding region as follows.

$$E_{\mathrm{UHF}} = \frac{E(UHF)-2\alpha}{U} = -2x^2 \left(x \leq {}^1/_2\right) \quad \text{(s8b)}$$

The orbital bifurcation point from RHF to UHF is given by $x = 1/2$, where the HOMO-LUMO energy gap (2β) becomes equivalent to the on-site repulsion integral U. This means chemically a conversion from a closed-shell bond, for example, hydroperoxide HO-OH, to an homolytic singlet diradical; HO•↑…↓•OH obtained by the O-O bond dissociation [35]. The situation is the same for the conversion from the closed-shell metal-metal (M-M) bond to the open-shell singlet M-M bond with the M•↑…↓•M character [35]. Therefore, the narrow HOMO-LUMO energy gap (Δε) obtained by the HMO model is also regarded as a chemical index for conversion from the non-radical to the diradical (magnetic) bond. The EPR spectroscopy has been used for experimental study of diradical species. The HOMO-LUMO mixing procedure [32] was applicable to obtain the UHF BS MOs in the instability region ($x \leq 1/2$) as illustrated in Fig. S1(a).

In 1970s, we have examined triangular three-center three electron [3e, 3o] and tetrahedral [4e, 4o] cluster models by using spin vector models as shown in Fig. S1(b) (see SI) [74, 76]. The triangular structure with the 120 degree of classical spin rotation was obtained for the [3e, 3o] model [74]. The tri-radical transition-metal clusters in Fig. S1 are referred to as the spin frustrated systems in quantum chemistry, indicating the extension of the different orbitals for different spins (DODS) into general spin orbitals (GSO), two component spinors (see Fig. S4) [35]. The BS methods indeed provide collinear and non-collinear spin structures for the triangular clusters [74] such as H_3 cluster.

UHF (DODS) and GHF (GSO) solutions for the triangular H_3 cluster model are shown in Fig. 3(a) [35, 74]. The potential curves of the H_3 radical by these solutions are shown in Fig. 3(b) in the main text, indicating that GHF (GSO) configuration is more stable than the UHF (DODS) configuration because of the spin frustration [74]. The resonating valence bond (RVB) model [71] has been proposed for quantum spins in spin frustrated systems. Similarly, the resonating BS (RBS) MO model [74] is feasible for spin-frustrated systems, providing the RBS configuration interaction (CI) scheme for quantum spins as shown in Fig. 3(b). The resonating (Res) GHF (GSO) CI state [82] is more stable than

the res UHF (DODS) CI state in the triangle H_3 model because of spin frustration. Thus, the concept of quantum resonance indicates that the spin projection (P) is crucial for low-spin GHF and UHF solutions (see Fig. S1). The approximate spin projection (AP) for low spin (LS) GHF and GHF [35] are performed by using the corresponding high-spin (HS) solutions as illustrated in Fig. S1(b).

Early theories examined for the [3e, 3o] model have been revived in recent discoveries of the triangular copper cluster and kagome cluster [75] and triangle $Cu(II)_3$ [5, 6] cluster in Fig. 1(c). The cubane-type [4e, 4o] cluster model [79] has also been revived in relation to Mn_4O_4 cluster [78] and London-model for OEC of PSII [83].

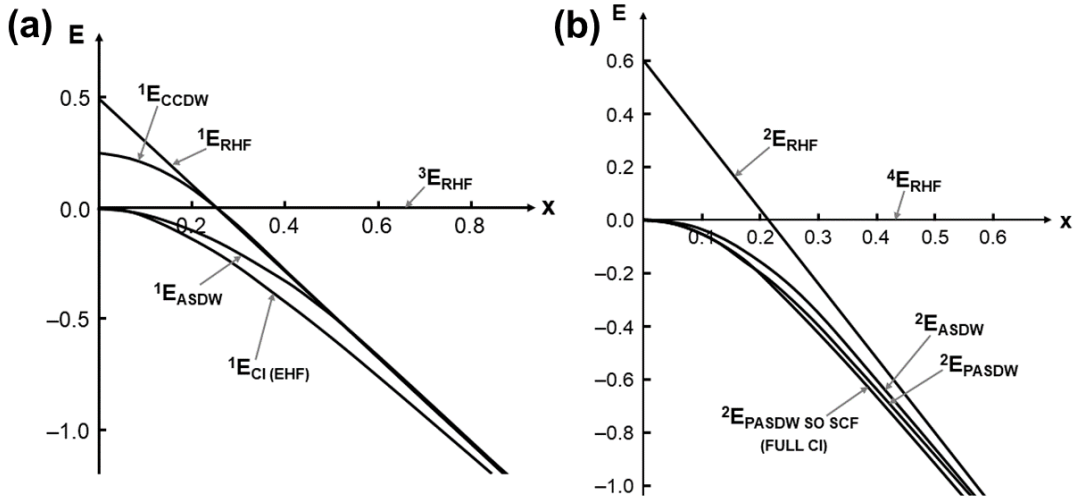

Fig. S1 The renormalized total energy curves by the RHF, UHF, EHF, and CI solutions on the basis of the Hubbard model for (a) two-center two electron [2e, 2o] and (b) three center three electron [3e, 3o] systems [31, 32]. The HOMO-LUMO mixing occurs in the region ($x < 1/2$) for (a). On the other hand, ^{2}RHF solution is unstable than ^{2}UHF for (b) in the whole region. CCDW denotes the complex charge-density-wave solution [23–25]. ASDW denotes the axial (collinear) spin density wave solution which is usually referred to as UHF SO SCF denotes the spin-optimized SCF.

SI.6 Functional dependences of chemical indices on the static electron correlations

Several chemical indices have been derived to elucidate the nature of chemical bonds of SCES. Functional dependence of them on the orbital overlap (T) is illustrated in Fig. S2. The spin density (Q_i) by BS is increasing sharply even in the strong orbital overlap region, where the diradical character (y_i) is relatively small. This characteristic feature is partly ascribed to the triplet spin contamination of the BS solution as discussed in the main text. The effective bond order (b_i) and information entropy (I_i) are

linearly decrease with the decrease of the orbital overlap (T_i). On the other hand, the diradical character (y_i) increases sharply in the small orbital overlap region, whereas the effective bond ($B_i = 1 - y_i$) after spin projection indicates the reverse tendency. Thus, functional dependence indicates the characteristic behaviors of the chemical indices for SCES.

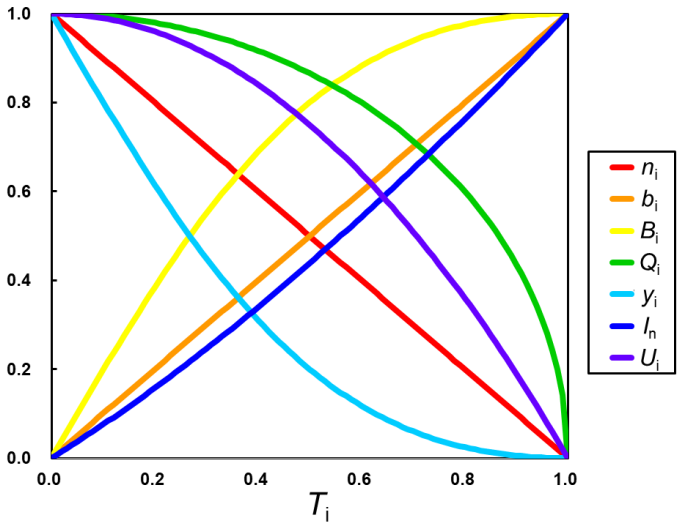

Fig.S2 Schematic illustration of variations of the chemical indices with the orbital overlap (T_i) between broken-symmetry (BS) orbitals in the BS methods coupled with spin projections. Spin density (green line) increase sharply even in the large orbital-overlap region (T_i = 0.7–0.8), indicating that several other chemical indices are examined to examine the nature of chemical bonds of SCES such as CaM_4O_5 cluster.

SI.7 Inter-relationship between symmetry-adapted and broken-symmetry methods

BS solutions involve the static electron correlations arising from the near orbital degeneracy as illustrated in Fig. S2. The natural orbital (NO) analysis of the BS solutions provides the natural orbitals (UNO) and their occupation numbers. The magnitude of the occupation numbers of UNO has been used for selection of complete active space (CAS) [88] for strongly correlated electron systems (SCES). UNO CAS configuration interaction (CI) is used for examination of scope and reliability of the BS solutions. The coupled-cluster (CC) single (S) method starting from UNO CAS CI [31] is formally regarded as UNO CASCF (= UNO CAS CCS) [88].

The dynamical correlation effects are very important to depict potential curves for SCES. The multi-reference UNO (MR) CI [31, 89] and/or second-order CI [31] have been proposed even in early days (1980) as shown in Fig. 4 in the main text. Moreover, UNO MR-CCSD has been also touched at that time [31]. However, such post BS methods have not been practical for complex large systems such as metalloenzymes even now. Therefore, as alternative practical procedures, hybrid DFT methods; BS MO +

BS DFT [64], have been used to investigate structure and bonding of the $CaMn_4O_x$ cluster [20].

The chemical indices in Fig. S2 are re-written with the occupation numbers of the natural orbitals (UNO) of BS solutions. Some of the chemical indices such as unpaired electron density are also expressed with the occupation numbers by the symmetry-adapted (SA) methods, namely MR CI and MR CC for strongly correlated electron systems (SCES) [31]. Therefore, chemical indices are regarded as common bridges between BS and post BS methods as illustrated in Fig. S3.

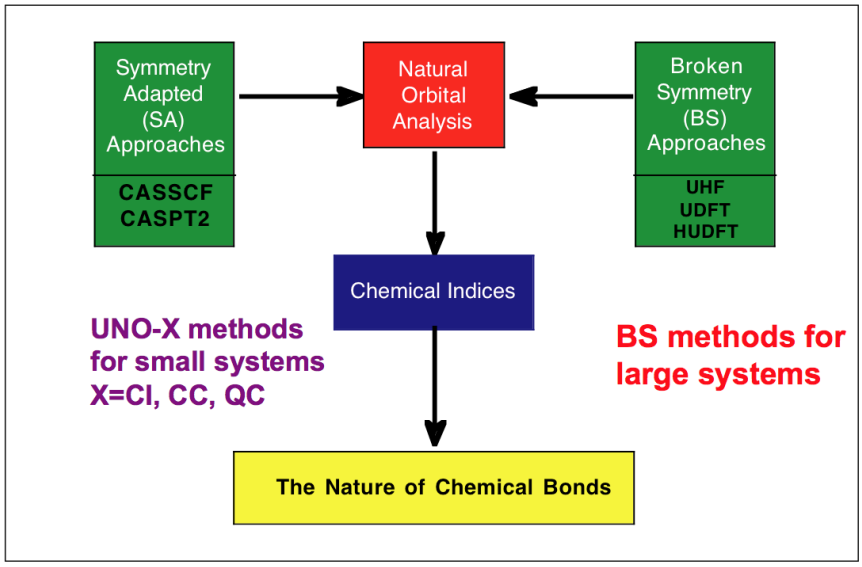

Fig. S3 The natural orbital (NO) analysis of the BS solutions provides natural orbitals (UNO) and their occupation numbers. The chemical indices in Fig. S2 are rewritten by using the occupation numbers of UNO. Some of the chemical indices are also expressed with the occupation numbers of the natural orbitals by the post BS methods, providing the conceptual bridges between BS and post BS.

SI.8 GSO-X (X = HF, DFT, hybrid DFT) program systems

In 1980s–1990s, chemical synthesis of multi-center transition-metal clusters with spin frustrations has been performed to obtain artificial catalysts for OEC of PSII: XMn_3O_4 and Mn_4O_4 [78]. However, complexes clusters with spin frustration could not be investigated by conventional program packages. Therefore, ab initio program packages for GSO-X (X = HF, DFT, hybrid DFT) [80–82] have been developed to elucidate structure and bonding of large transition metal complexes with spin frustrations as illustrated in Fig. S4. The closed-shell state is described by the restricted Hartree-Fock (RHF) [46] or restricted DFT (RDFT) solution. On the other hand, one (1D), two (2D), and three (3D) dimensional spin structures are described by the 1D UHF, 2D Helical SDW(HSDW), and 3D torsional DFT(TSDT) solutions, respectively [77, 79]. The general spin structures for systems under consideration are first

obtained by the spin vector model [74] which is characterized by the magnetic group (spin rotation (S) × time-reversal (T)) symmetry) as illustrated in Fig. S4. On the other hand, special symmetry-adapted (P_n) molecular orbitals (MO) for the systems are obtained by the extended Hückel MO (EHMO) methods [41]. Therefore, general spin orbitals (GSO) for them are constructed by the HOMO-SOMO-LUMO mixing using the magnetic double group theory ($P_n \times S \times T$). The SCF calculations for trial GSO obtained were performed to obtain GHF solutions with desired magnetic double group theory [77–82]. The GSO HDFT is applicable to elucidate structure and bonding of multi-center clusters with spin frustrations (see Fig. 1(c)).

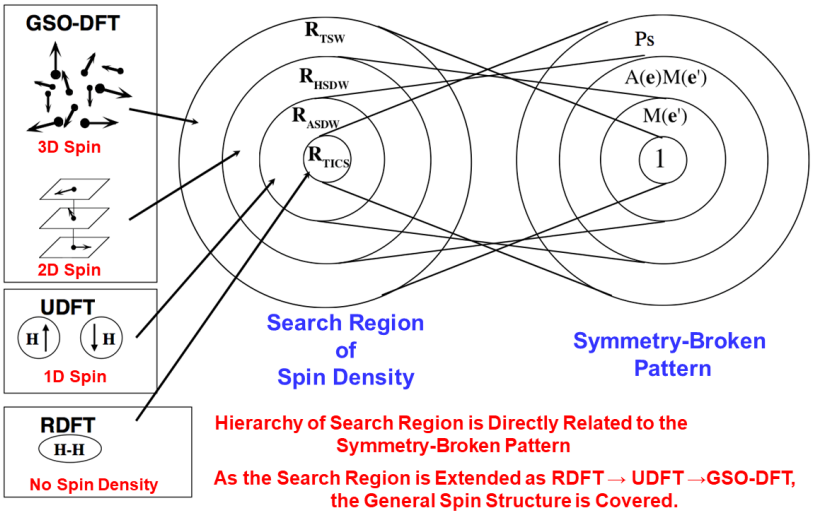

Fig. S4 Collinear and non-collinear broken symmetry (BS) solutions classified by the magnetic double groups [77, 79–82].

SI.9 Ab initio GSO computations for manganese clusters with spin frustration

As mentioned above, UHF solution with the axial (collinear) spin alignment for spin frustrated systems suffered the spin flip instability, reorganizing into the more stable GHF solution [35, 80–82] consisted of two component spinor (GSO)), which is accord with the triangular (non-collinear) two-dimensional (2D) spin alignment. Figure S1(b) illustrates the normalized energies of the [3e, 3o] quantum systems by GHF with GSO, projected (P) GHF (PGHF), and extended Hartree-Fock (EHF) [67]. The spin vector model for the [4e, 4o] model has provided the tetrahedral three-dimensional (3D) spin structure [76–78]. The potential curves for the [4e, 4o] model have also been obtained with GHF, PGHF, and EHF with GSO [78], supporting the 3D spin structure [67, 74]. In 1970s, RHF, UHF (1D) and GHF (2D, 3D) solutions have been theoretically examined for SCES with spin frustration. Thus, the molecular orbital descriptions of complex radicals are feasible under the general BS approximation in general (see Fig. S4).

Interestingly, the [3e, 3o] cluster was involved in the London model [83] of the $CaMn_4O_4$ cluster in the S_1 state of the Kok cycle [37] for water oxidation. Ab initio GSO DFT computations [84] for the London model consisted of the regular cubane $CaMn_3O_4$ structure plus dangling Mn structure [83] have indeed elucidated the greater stability of GHF (non-collinear) than UHF (collinear) solution. On the other hand, the reduction of GHF to UHF has been concluded for the $CaMn_3O_4$ cluster observed by HR XRD [8] because of the distorted cubane structure. The triangular Cu(II) complexes [5, 6] for mono-oxygenations of methane in Fig. 1(c) is also a typical example of the [3e, 3o] system. Solomon's group has extensively investigated structure, bonding, and reactivity of tri-copper enzymes in Fig. 1 [5, 6].

Cubane structures have been observed for iron-sulfur clusters in biological systems such as PSI system [21, 77]. Possible collinear and non-collinear BS solutions for the cubane-like clusters such as Fe_4S_4 in photosystem I (PSI) were constructed by the magnetic double group consisted of spatial symmetry (P_n), spin rotation (S) and time-reversal (T) symmetry ($P_n \times S \times T$) (see Fig. S5) [80–82]. GSO DFT computations [81] have also performed for the regular cubane Mn_4O_4 cluster with the tetrahedral spin structure, which is regarded as a model of artificial catalysts for water oxidation by Dismukes group (Fig. S5(d)) [78]. Thus, GHF and GSO DFT solutions with one (1D), two (2D), and/or three (3D) dimensional spin structures are obtained as true ground states at the BS level of theory [23–25, 34] for complex transition metal complexes based on the magnetic double group ($P_n \times S \times T$) theory [80–82]. Magnetic materials with triangular structures have been also investigated in the material science [35, 73]. The copper kagome antiferromagnets [75] for water oxidation have indeed attracted great interest in relation to spin liquid state [73]. This in turn indicates that 3d-transition metal clusters (M = Cu, Mn, Fe, Co, etc.) with spin frustration might be useful for catalysts of artificial photosynthesis [20]. In fact, $Mn_{12}O_{12}$ complexes were found to be effective catalysts for water oxidation [20]. Designs of coordination ligands to the clusters are important for stabilization of the earth abundant 3d-metal cluster complexes and controls of redox potentials as discussed in the final section of this paper. In PSII and C*c*O, protein matrix acts effectively for these important factors, suggesting importance of coordination ligands for artificial systems.

As mentioned above, Barber et al. [83] have proposed the so-called London model, regular cubane-like $CaMn_3O_4$ with the dangling Mn site as illustrated in Fig. S5(e). Interestingly, the Mn-Mn distances of the cubane-like $CaMn_3O_4$ cluster were similar, indicating the triangular-type geometrical structure [84, 85]. In fact, we have obtained the stable GSO solution with the triangular spin structure (Fig. S5(g)) [84]. This means no Jahn-Teller (JT) distortion of the regular cubane-like $CaMn_3O_4$ cluster with the uniform valence state, $Ca(II)Mn(X)_3O_4$ (X = II or IV) in contradiction to the low- and high-oxidation scenarios with the JT Mn(III) ion [8]. Thus, the orbital degree of freedom (JT effect) is one of the

important factors for understanding and explanation of subtle geometry change of the $CaMn_4O_x$ cluster in PSII. The total and orbital spin densities obtained by the BS computations are useful for elucidation of the valence configurations of Mn ions and the JT effect by the Mn(III) ion in PSII (see Fig. S5). At the moment, active and robust artificial Mn oxide clusters with Mn(III) site are not synthesized [78], suggesting importance of active control of the JT distortion.

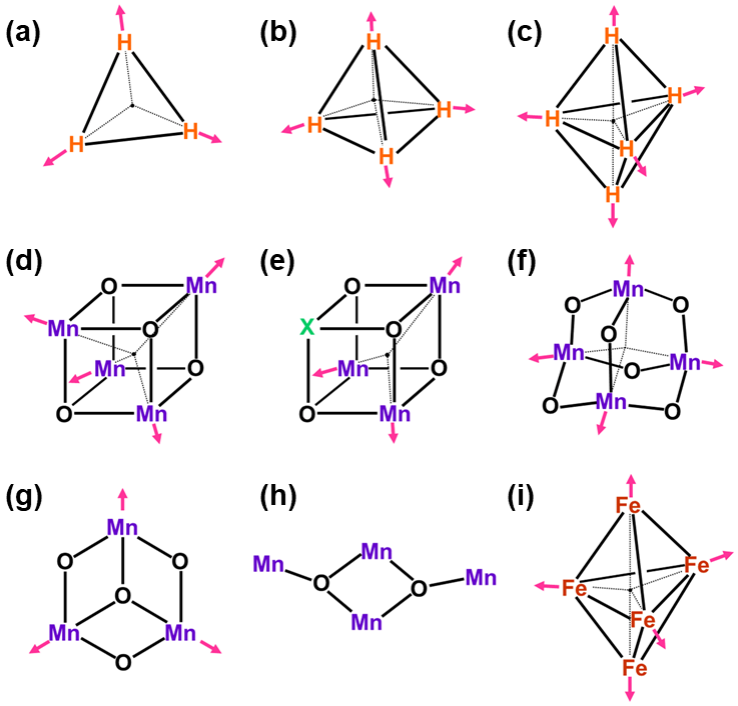

Fig. S5 Hydrogen atom, Mn, and Fe cluster models with spin frustrations. Antiferromagnetic (AF) exchange interactions are expressed with arrow notations.

SI.10 Dynamical electron correlations for chemical bonding energies and potential curves

The MO symmetry- and broken- symmetry orbital pictures based on the independent particle models [32, 35] derived from the instability condition [23–25] are useful for qualitative understanding and explanations of radical reactions in addition to theoretical investigation of the non-dynamical electron correlation effects arising from the near orbital degeneracy as illustrated in Figs. S4 and S5. On the other hand, dynamical correlation effects are inevitably included for quantitative purposes as illustrated in Fig. 4 in the main text, indicating the necessity of the post RHF and UHF methods.

To this end, in 1950s, Coester and Kümmel [26, 27] already developed the coupled-cluster (CC) methods in nuclear physics. In 1966, Čížek [28] and later together with Paldus et al. [29], have reformulated the CC methods for inclusion of correlation effects in atoms and molecules, providing the

RHF CC and UHF CC approaches based on the exponential ansatz (e^T) where T (= $T_1 + T_2 + T_3 + \ldots$) denotes the cluster operator consisted of single (S = T_1), double (D = T_2), triple (T = T_3), higher excitations as illustrated in Fig. 4. The CC SDT and CCSD(T) methods [28–30] are now standard procedures for inclusion of electron correlation effects in quantum chemistry.

The stability condition was used for selection of appropriate reference function for the CC approach in our approach, providing the general Hartree-Fock (GHF) (RHF, UHF, GHF with two component spinor, etc.) wavefunction for the single reference (SR) CC. The natural orbital analysis of the UHF solutions provides the natural orbitals (UNO) and their occupation numbers, which are used for construction of the [*n*e, *m*o] multi-reference (MR) zero-order function [31, 35]. Therefore, UNO MR [n, m] CCS has been mathematically equivalent to UNO [*n*e, *m*o] CASSCF [88]. However, full valence MCSCF was the dream at that time. The UNO MR [*n*e, *m*o] CCSD was too difficult at that time, and therefore UNO MR [*n*e, *m*o] CI followed by Davidson correction [89] was performed alternatively [31].

The UNO of the HFS solutions was proposed for MR CCSD approach for metal clusters [90] although the trial function does not satisfy the Brillouin's theorem [31]. The situation is the same for DLPNO CCSD(T_0) method [68, 69] which uses the UNO (LNO) of HDFT methods (see later). Figure 4 illustrates our computational schemes for SCES [31]. As shown in section III, the DLPNO can be obtained for small molecules by the UHF computations in the UHF CCSD(T) scheme. However, UHF CCSD(T) computations are hardly possible for the metalloenzymes in Fig. 1, indicating the necessity of the DLPNO-CCSD(T_0) by the use of UNO (LNO) for practical purpose [70–72]. The computational results by DLPNO-CCSD(T_0) have been used to elucidate scope and reliability of those of the HDFT methods [20]. In this paper, DLPNO-CCSD(T_0) computations are newly applied to a large QM model for the $CaMn_4O_x$ cluster in the S_4 state. The computational results at this level are found to be useful for present purpose in section VI and VII.

SII Spin Hamiltonian models for strongly correlated electron systems

SII.1 Dirac identity and Heisenberg Spin Hamiltonian model for bi- and poly-nuclear systems

In early 1970s, both spin-free [105] and spin-dependent models [74, 102] were proposed for theoretical modeling of radical reactions. In many electron systems the exchange of the electron spin is of fundamental importance [102]. Over past decades, spin Hamiltonian models [102] have been employed to elucidate effective exchange interactions of SCES [104] in material science. Chemical reactivity of SCES with local spins in molecules has been also attracted great interest in the field of chemistry. The BS models are often mapped into the Heisenberg spin Hamiltonian model [102] through the transformation from the canonical orbital to localized orbitals [35, 106] for exchange-coupled open-shell species. To this

end, the scalar product of the spin is considered as follows [35, 86]:

$$S_i \cdot S_j = \frac{1}{2}\left[\left(S_i + S_j\right)^2 - S_i^2 - S_j^2\right] \quad \text{(s9)}.$$

The expectation value of the scalar product is given by the singlet and triplet diradicals as follows:

$$^1\langle S_i \cdot S_j\rangle = \frac{1}{2}\left[0(0+1) - \frac{1}{2}\left(\frac{1}{2}+1\right) - \frac{1}{2}\left(\frac{1}{2}+1\right)\right] = -\frac{3}{4} \quad \text{(s10a)},$$

$$^3\langle S_i \cdot S_j\rangle = \frac{1}{2}\left[1(1+1) - \frac{1}{2}\left(\frac{1}{2}+1\right) - \frac{1}{2}\left(\frac{1}{2}+1\right)\right] = \frac{1}{4} \quad \text{(s10b)}.$$

Therefore, the permutation operator P_{ij} [103, 105] can be defined by the spin scalar product.

$$^1P_{ij} = {}^1\langle 2S_i \cdot S_j + \frac{1}{2}\rangle = 2x\left(-\frac{3}{4} + \frac{1}{2}\right) = -1 \quad \text{(s11a)},$$

$$^3P_{ij} = {}^3\langle 2S_i \cdot S_j + \frac{1}{2}\rangle = 2x\left(\frac{1}{4} + \frac{1}{2}\right) = 1 \quad \text{(s11b)}.$$

The above relationship is called as the Dirac identity [103], indicating the direct relation between the permutation operator in the valence bond (VB) model [104] and the spin operators in the spin Hamiltonian model [102]. Dirac identity [103] is the theoretical foundation for the spin-free approach to radical reactions by Matsen and his collaborators [105] in a sharp contrast to our spin-dependent approach [35, 74, 86].

The BS MO model in the weak bond region is often transformed into the spin Hamiltonian model [35, 62, 107] based on the second quantization formula of the spin operator S_i.

$$H_{ij} = -2J_{ij}S_i \cdot S_j \quad \text{(s12)}.$$

where J_{ij} is the effective exchange integral. The total energies of the singlet and triplet states of the binuclear open-shell systems on the Heisenberg model [102] are given by

$$^1E_{spin} = {}^1\langle H_{ij}\rangle = \frac{3}{2}J_{ij},\ {}^3E_{spin} = {}^3\langle H_{ij}\rangle = -\frac{1}{2}J_{ij} \quad \text{(s13a)}.$$

The energy gap between the singlet and triplet states is given by

$$ {}^{1}E_{\mathrm{spin}} - {}^{3}E_{\mathrm{spin}} = 2J_{ij} \quad . \qquad \text{(s13b)}, $$

where equation (s13b) for the *J* value is often referred to as the chemist's notation.

The above two spin model can be generalized in the case of the multi-electrons A and B at the sites a and b, where A (B)-electrons are parallel at the a (b) site, namely the local high-spin configurations. The effective exchange integrals defined by each orbitals (i, j) are approximated by the orbital averaged exchange integrals as follows [35, 62]:

$$ H_{ab} = -2\sum_i \sum_j J_{ij} S_i \cdot S_j = -2J_{ab} S_a \cdot S_b \ , \qquad \text{(s14a)}, $$

where

$$ S_a = \sum_i S_i \ (i = 1, 2, \cdots, A), \ S_b = \sum_j S_j \ (j = 1, 2, \cdots, B) \qquad \text{(s14b)}. $$

Therefore, the Heisenberg models for polyradical species [35, 62, 107] are generally given by

$$ H = -\sum_{a>b} 2J_{ab} S_a \cdot S_b, \qquad \text{(s15)}, $$

where J_{ab} is the orbital-averaged effective exchange integral between the spin sites a and b with total spin operators S_a and S_b. The exact diagonalizations of the spin Hamiltonians provide energy levels and projection factors for molecular quantum spins [21] which are used for explanation and understanding of the EPR experimental results [108].

The Mn(III) and Mn(IV) ions in the $CaMn_4O_x$ cluster in OEC of PSII are local high-spin, indicating i = 4 and 3 in eq, (s14b), namely S_a = 4/2 and S_a = 3/2, respectively. The total local spin models are applicable to express spin structures of the Mn(III) and Mn(IV) ions, providing the spin Hamiltonian model with the orbital average effective exchange integrals in eq. (s15). The exact diagonalization of the spin Hamiltonian matrix provides the quantum-mechanical energy levels and projection factors of spin populations which are used for analysis of the EPR results [108].

SII.2 Ab initio calculations of effective exchange integrals for metalloenzymes

Historically, magnetic susceptibility experiments and EPR experiments have been performed to elucidate

the exchange coupling between transition metal ions in metalloenzymes [35, 62, 86]. The spin Hamiltonian models given in eq. (s15) were employed for analysis of the observed temperature dependent paramagnetism [35, 62, 86] even for transition metal complexes with the total singlet ground state [107]. The observed paramagnetism was qualitatively compatible with the BS model [35, 62]. Therefore, we have derived computational schemes of J_{ab} parameters by using total energies (^{X}E) of BS solutions for the low-spin (LS) and high-spin (HS) configurations as follows [62, 107]:

$$J_{ab} = [^{LS}E - {}^{HS}E] / [^{HS}\langle \boldsymbol{S}^2 \rangle - {}^{LS}\langle \boldsymbol{S}^2 \rangle] \ . \qquad \text{(s16a)}$$

The $^{X}\langle \boldsymbol{S}^2 \rangle$ denotes total spin eigenvalue for the spin state X. The total energy of the spin projected UHF (PUHF) (see Fig. 3(b)) is given by the following equation.

$$^{LS}E_{PUHF} = {}^{LS}E_{UHF} + J_{ab} [^{LS}\langle \boldsymbol{S}^2 \rangle - S(S+1)] \ . \qquad \text{(s16b)}$$

where $S(S+1)$ denotes the exact eigenvalue of the total spin density operator. Therefore, the second term in eq. (s16b) corresponds to the spin correction term for spin contamination in BS model [35].

The J_{ab} parameters calculated for the M-X-M and MX_2M ($X = O^{2-}$, OH^-) were compatible with available experimental results [35, 62, 86, 107]. The J_{ab} parameters for the Mn-O-Mn with shorter Mn-Mn distances than 3.0 Å were negative in sign, indicating the antiferromagnetic (AF) exchange interaction [62]. On the other hand, spin crossover from AF to ferromagnetic (FR) ground state for longer Mn-Mn distances than 3.0 Å, indicating similar behavior of the J_{31} parameter in $CaMn_4O_x$ (see Fig. 1). As shown in the ref. [86], BS methods are handy and practical for theoretical computations of the six J values for $CaMn_4O_x$. Thus, the EPR experiments [108] have provided crucial information for elucidation of electronic and spin structures of SCES such as $CaMn_4O_x$.

SIII structure and bonding of the $CaMn_4O_5$ cluster in OEC of PSII

SIII.1 Jahn-Teller distortion of the $CaMn_4O_x$ cluster

In 2003, GSO DFT computations were performed for the Mn_4O_4 cluster with the uniform cubane structure without the JT distortion (Fig. S5(d)) [81]. In 2004, the XRD structure (London model) by Barber et al. [83] has provided the regular cubane-like $CaMn_3O_4$ structure with the triangle Mn_3 skeleton with the triangle spin structure (Fig. S5(e)) [74]. This means no JT distortion of the Mn(III) ion, indicating $Mn(II)_3$ or $Mn(IV)_3$ clusters. However, judging from the valence structure ($Mn(III)_2Mn(IV)_2$) in the S_1 state, such uniform valence structure resulted from the XRD structure [83] was unreasonable,

indicating the necessity of further refinements [86]. The high-resolution (HR) XRD structure by Umena et al. [8] indeed has elucidated the distorted-chair like structure in the dark stable S_1 state, indicating the possible role of the Mn(III) ion for such distortion. Thus, the HR XRD structure [8] has provided structural foundation for structure and bonding of the $CaMn_4O_5$ cluster in OEC of PSII.

SIII.2 Structure and bonding of the $CaMn_4O_x$ cluster

The $CaMn_4O_5$ cluster is regarded as one of typical strongly correlated electron systems (SCES) which exhibit spin, charge, and orbital degrees of freedom based on the viewpoint of chemical physics. For example, eight different spin structures are conceivable for the four spin clusters as shown in Fig. S6(a). On the other hand, six different valence structures are feasible for the $Mn(III)_2Mn(IV)_2$ cluster in the S_1 state as illustrated in Fig. S6(b). Therefore, total 48 (= 8 × 6) spin-charge structures are conceivable for the S_1 state as illustrated in Fig. S6(c).

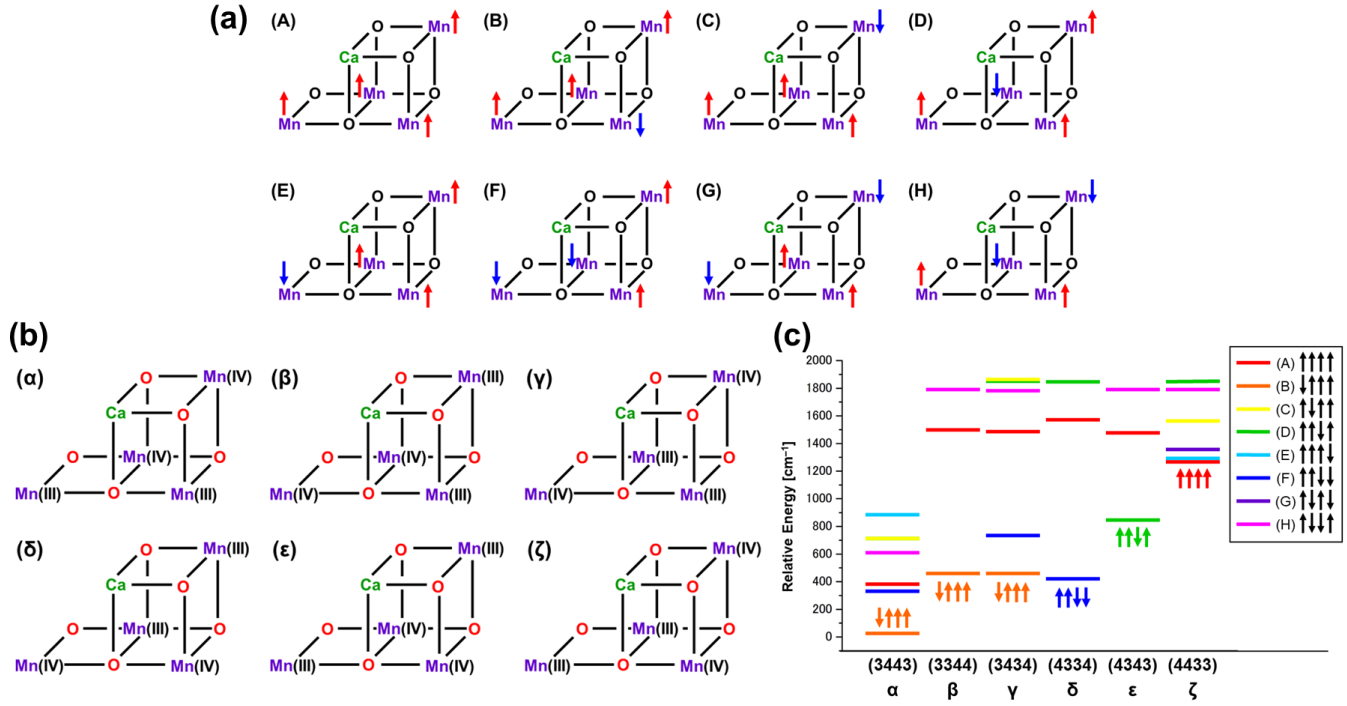

Fig. S6 (a) Possible eight spin structures for the $CaMn_4O_5$ cluster in OEC of PSII and (b) possible six different valence structure of the $CaMn_4O_5$ cluster in OEC of PSII, and (c) Total spin-charge configurations for the $CaMn_4O_5$ cluster in OEC of PSII.

The relative energies obtained by the UB3LYP level of theory elucidated the largest stability of the S_1 configuration with the (3443) valence state under the assumption of the HR XRD structure [8]. However, the ground S_1 spin structure with (3443) was $S = 3$ in contradiction to the observed $S = 0$ state

by EPR [20]. Therefore, the full geometry optimizations of the HR XRD structure were inevitable to obtain the refined structure of the S_1 state as shown in Fig. 6 in the main text. The refined structure for the S_1 state was found to be consistent with the SFX XFEL results [17, 18]. The HDFT computations were performed to obtain geometric structures of the S_2, S_3, and S_0 states as shown in Fig. 7 [87]. These predicted structures [87] were found to be consistent with those of the SFX-XFEL experiments [17, 18]. Thus, geometry optimizations by HDFT methods are useful enough for structure determinations.

SIV Relative stabilities among the S_3 intermediates by DFT and beyond DFT

As mentioned above, HDFT was effective for full geometry optimizations of $CaMn_4O_5$ cluster in the S_3 state. However, elucidation of relative energies among S_3 intermediates was a difficult task at HDFT level of theory as compared with the geometry optimizations (see Fig. 5) [20, 66]. Therefore, beyond HDFT computations such as the coupled cluster (CC) model are desirable as shown in Fig. 4 in the text. Theoretically, UHF solution has been used as the UHF coupled cluster (CC) SD(T) computations (UCCSD(T)) as shown in Fig. 4. The UCCSD(T) computations are feasible for medium size organic radicals. On the other hand, UHF SCF computations are often hardly converged in the case of large transition metal oxides such as $CaMn_4O_6$ cluster. Alternately, unrestricted Hartree-Fock-Slater (UHFS) methods have been used for such complex systems [50]. In fact, UCCSD computations starting from UHFS solution has been proposed as an approximate procedure for metal clusters [50]. The UHFS method is considered as a precursor method for hybrid DFT (HDFT) method that is applicable even for $CaMn_4O_6$ cluster. Trial localized natural orbitals (ULO) by HDFT are indeed very important for effective and practical DLPNO-CCSD(T_0) computations for open-shell clusters [68, 69].

The ULO obtained by the localization of the canonical UNO by UB3LYP are used for trial orbitals in our DLPNO-CCSD(T_0) computations as shown in Fig. S7. We have performed the normal (*n*-) PNO DLPNO-CCSD(T_0) computations using trial ULOs obtained by UB3LYP (w = 20%), UB3LYP* (w = 15%), and UB3LYP*** (w = 10%) methods as shown in Fig. S7. Relative energies for each intermediate by *n*-PNO DLPNO-CCSD(T_0) are not so different among trial ULOs employed because of the orbital optimization by the CC single (S) excitation process. This in turn means the ULOs by HDFT are useful for trial NOs for the DLPNO-CCSD(T_0) computations. Therefore, UNO by UB3LYP (w = 20%) (see Fig. S1) has been used for practical trials for the ULO DLPNO-CCSD(T_0) computations of total energies of possible intermediates in the Kok cycle for water oxidation in eq. (1) [20, 70–72]. Relative energies among the S_3 intermediates were variable as shown in Fig. S6, indicating strong dependence of the weight (w) of the Hartree-Fock exchange term in the UB3LYP computations (w = 10–20%). Therefore, DLPNO-CCSD(T_0) results are crucial for elucidation of scope and reliability of relative energies by the HDFT results.

DLPNO-CCSD(T_0) by use of UNO [31] were found to be effective for elucidation of relative energies among the S_3 intermediates. However, the previous DLPNO-CCSD(T_0) computations [70–72] were based on small QM model (103 atoms), which were not regarded Tyr161 radical site. This means such small QM model is not appropriate for theoretical investigation of possible intermediates in the early S_4 state : [S_3 + Tyr-O radical] configuration. In this paper, an extended QM (283 atoms) model has been constructed for the S_3 state as illustrated in Fig. 8 in the main text. HDFT and DLPNO-CCSD(T_0) computations based this model are performed to elucidate the relative stability between [S_{3abca}(R)-OH + Tyr-O radical] and [S_{3acca}(R)-Peroxide + Tyr-O radical]. The computational results are given in the main text.

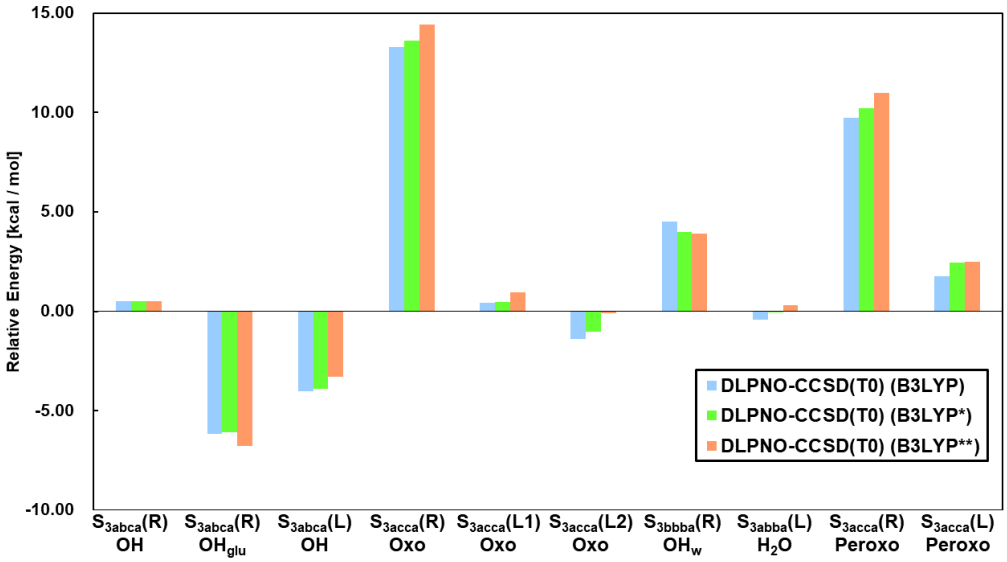

Fig. S7 Relative energies among the S_3 intermediates by *n*-DLPNO CCSD(T_0) computations using trial ULOs obtained by UB3LYP (w = 20%), UB3LYP* (w = 15%), and UB3LYP*** (w = 10%) methods.

SV Extended Kok cycle

SV.1 Photo-induced hole doping in PSII

Photosynthesis is one of the most important photochemical reactions. Photosynthesis is initiated by the photo-induced one electron transfer (OET) from P680 pigment to plastoquinone A (Q_A), providing an electron transfer (ET) diradical examined in section III in the text as shown in eq. (ET-1). The generated $P680^{+}$• cation radical acts effectively as the one electron acceptor for Tyr161-OH, providing Tyr161-OH^{+}• cation radical as illustrated in eq. (ET-2). In PSII, His190 becomes a proton acceptor for the Tyr161-OH^{+}• cation radical, affording the tyrosine oxygen radical Tyr161-O• as shown in eq. (PT-1). The generated Tyr161-O• can abstract one electron from the catalytic cluster $CaMn_4O_x(H_2O)_4$, providing the

one-hole doped $CaMn_4O_x(H_2O)_4^{+}$• state, where a hole is introduced in manganese ions in the Kok cycle for water oxidation. On the other hand, the generated tyrosine oxygen anion Tyr161-O^{-} accepts a proton from the protonated histidine cation H^{+}-His190, providing the neutral Tyr161-OH and His190.

$$P680 + h\nu + Q_A \rightarrow P680^{+}\bullet + Q_A^{-}\bullet \quad \text{(ET-1)}$$

$$P680^{+}\bullet + \text{Tyr161-OH} \rightarrow P680 + \text{Tyr161-OH}^{+}\bullet \quad \text{(ET-2)}$$

$$\text{Tyr161-OH}^{+}\bullet + \text{His190} \rightarrow \text{Tyr161-O}\bullet + H^{+}\text{-His190} \quad \text{(PT-1)}$$

$$\text{Tyr161-O}\bullet + CaMn_4O_x(H_2O)_4 \rightarrow \text{Tyr161-O}^{-} + CaMn_4O_x(H_2O)_4^{+}\bullet \quad \text{(ET-3)}$$

$$\text{Tyr161-O}^{-} + H^{+}\text{-His190} \rightarrow \text{Tyr161-OH} + \text{His190} \quad \text{(PT-2)}$$

The net process is regarded as a photo-induced one ET from the catalytic cluster $CaMn_4O_x(H_2O)_4$ to plastoquinone A (Q_A) in PSII. Therefore, four times photo-excitations are required to dope four holes in the $CaMn_4O_x(H_2O)_4$ for water oxidation in eq. (1) in the main text. Deprotonations (oxidation) of the coordinated water molecules through proton release pathways (PRP) are also essential for controls of the redox potentials for one ET from the cluster to Tyr161-O• in the ET-3 step.

SV.2 Five steps for water oxidation in the Kok cycle

The Kok cycle for water oxidation in PSII [37] is usually expressed with the five steps (S_i = 0–4) for which the valence states of the four Mn sites are given as follows; (3433), (3443), (3444), and (4444) for S_0, S_1, S_2, and S_3 states under the high-oxidation scenario, respectively. However, Tyr-O• radical is formed in each transition from S_i to S_{i+1}. Therefore, the Kok cycle [37] is extended to include the intermediate stage where the Tyr161 radical (Tyr-O•) is formed as illustrated in Fig. S8. In the extended Kok cycle, the S_3+ Tyr-O• radical stage is particularly important for elucidation of the mechanism of the O-O bond formation as discussed in the main text.

The high-valent state (5444) or formation of the oxyl-radical configuration (4444)-O• is often assumed for the S_4 state [1, 2]. The conventional acid base (AB) mechanism is conceivable for the (5444) state, whereas the radical coupling (RC) mechanism is conceivable for the (4444)-O• state as shown in eq. (7) in the main text. On the other hand, the PCET or NA-one ET mechanism is feasible in participation with the Tyr-O• radical for the O-O bond formation for water oxidation in PSII without the formation of the Mn(V)=O or •Mn(IV)-O• bond [20] as in the case of no formation of Fe(V)=O bond in C*c*O [3,4]. Unfortunately, variations of the valence state in the $S_3 \rightarrow [S_4] \rightarrow S_0$ transition in PSII have not been reported yet [116–119]. On the other hand, the EPR results have been reported for C*c*O [122–140]. Therefore, the iso-lobal and iso-spin analogy between PSII and C*c*O have been assumed as illustrated in Fig. 13 in the main text.

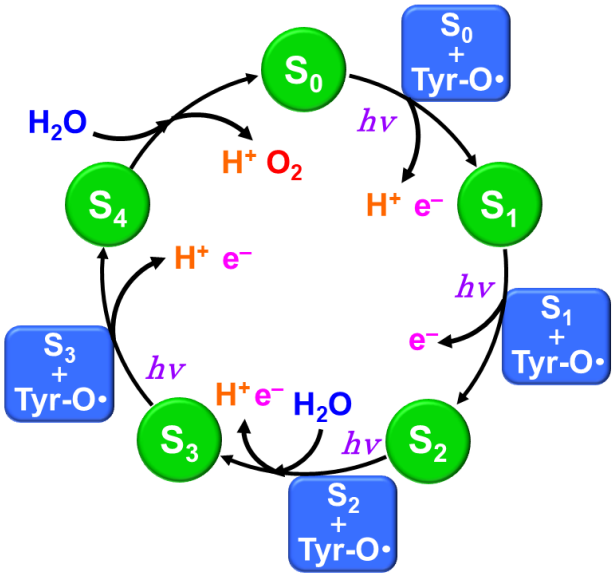

Fig. S8 Kok cycle [37] for water oxidation in OEC of PSII; One electron oxidation of the $CaMn_4O_5$ cluster occurs four times for the formation of total four holes formation for water oxidation. The valence and spin states of the $CaMn_4O_5$ cluster are shown under the assumption of the high-oxidation scenario for the S_i (i = 1–4) states, namely the $Mn(III)_2Mn(IV)_2$ valence state for the dark stable S_1 state. Possible pathways for water inlet and proton release in the Kok cycle are discussed in this supporting material.

SV.3 Proton transfer coupled electron transfer (PT-ET) processes in PSII

PT-ET concepts in section III are applicable for understanding of the molecular mechanisms of the Kok cycle for water oxidation under the 4H model [87]. The one-electron transfer (ET) and proton transfer (PT) reactions take place for the photo-induced conversion from the S_0 to the S_1 state, in turn providing the one-electron reduced Mn valence state and one protonated oxygen dianion site for the S_0 state: the $Ca(II)Mn(III)_3Mn(IV)_1O_4(OH^-)(H_2O)_4$ [21]. Full geometry computations have revealed the (3433) valence state for the S_0 state and two protonation sites $O_{(5)}$ and $O_{(4)}$, providing the S_{0bcca} and S_{0accb} isomers. The PC-ET reactions are expected to the conversion from the S_1 to S_2 state, providing the $Ca(II)Mn(III)_1Mn(IV)_3O_5(OH^-)(H_2O)_3$. However, experimental investigations have revealed no proton release to lumen in the S_1–S_2 transition [1]. Therefore, we have assumed proton-trapping by a base (B) site near $CaMn_4O_5$ cluster, providing the BH^+ (see Fig. 9) [20]. Full geometry optimizations by HDFT have revealed that right (R)- and left (L)-opened structures are feasible for the S_2 state, providing the S_{2acca}(R) structure with the (3444) valence state and the S_{2abca}(L) structure with the (4443) valence state [87, 111]. Relative stability between the S_2 isomers was calculated to be small by the quantum mechanics (QM) calculations [87]. The situation was the same for the so-called 3H models, S_{2abca}(R) with (3444) and

S_{2abca}(L).

The PT-ET scheme in Fig. 5 was also expected to the conversion from the S_2 to S_3 state, providing the Ca(II)Mn(IV)$_4$O$_5$(OH$^-$)$_2$(H$_2$O)$_2$, namely S_{3abba}(R) and S_{3abba}(L) where X = U = O^{2-}, Y = Z = OH^- in Fig. 6. Past decades, experimental results [1] have suggested the insertion of extra water molecule (W_{INT} = W) into the reaction site in the S_2 to S_3 transition. Therefore, HDFT computations [87] have been performed to elucidate the S_3 structures after water insertion. Full optimized geometries of both right (R)- and left (L)-opened S_3 structures were obtained, indicating that the Ca(II)Mn(IV)$_4$O$_5$(OH$^-$)$_2$(H$_2$O)$_3$, namely S_{3abca}(R)-OH with (4444) where X = U = O^{2-}, Y = OH^-, W = OH^- is the most stable among the S_3 intermediates as illustrated in Fig. S9 [115].

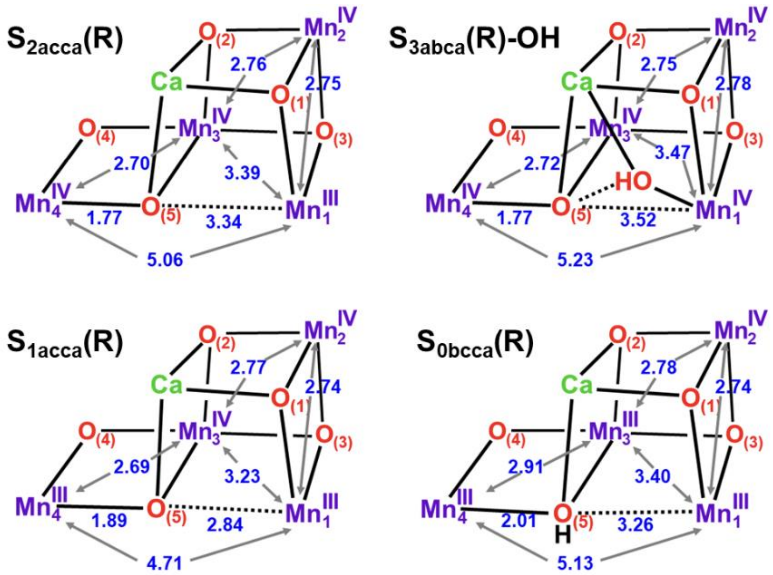

Fig. S9 The full optimized geometry [87] of the S_1 state starting from the HR XRD structure [8]. The optimized structures for the S_2, S_3, and S_0 structures starting from the optimized S_1 structure are also given, showing water insertion at the S_2 to S_3 transition in the Kok cycle. The predicted geometric structures by QM [87] are now compatible with the observed results by SFX XFEL [17, 18, 116–119].

SV.4 Examination of a new model for the O-O bond formation by SFX XFEL results

As shown in Fig. S9, water oxidation reaction in the Kok cycle of PSII are consisted of three important processes, (a) proton transfer (PT), (b) electron transfer (ET), and O-O bond formation from water molecules. Recent time-resolved (TR) SFX-XFEL experiments have elucidated timing of these three steps. According to the recent TR SFX-XFEL experiments [116–120] on the S_2 to S_3 transition, formation of Tyr161-O• in the ET-1 to PT-1 processes proceeded within 50 μs in conjugation with the change of

H-bond network along the residues Tyr161-His190-Asn298. After the rapid formation of Tyr161-O•, the proton release (PR) was observed after 150 μs later for the second flash. On the other hand, the one ET from $CaMn_4O_x(H_2O)_4$ to Tyr161-O• in eq. (ET-3) occurred after 250 μs later for the second flash, indicating a sequential step in the PT-ET process. Water insertion ($O_{(6)}$ or O_X) was initiated after the formation of the (4444) valence state in the S_3 state, where O_X denotes, O^{2-} or HO^- since hydrogen atom is invisible by XRD and SFX XFEL.

The TR SFX XFEL experiment [116–119] has also provided critical information on the so-called lag phase in the S_3 to S_0 transition through S_4 transition state. The formation of Tyr161-O• in the ET-1 to PT-1 processes proceeded within 50 μs in conjugation with the change of H-bond network along the residues Tyr161-His190-Asn298 even in this step. After the rapid formation of Tyr161-O•, the proton release (PR) was observed after 200–500 μs later for the third flash, indicating a similar process to that of the S_2 to S_3 transition. Interestingly, above-mentioned three events, (a) reduction of Tyr161-O•, (b) one electron oxidation of the $CaMn_4O_x(H_2O)_4$, and (c) O-O bond formation, were found to take place in the next stage within 500 to 1200 μs. The TR SFX-XFEL results [116–119] have also elucidated that the onset of the O_2 release occurs after 730 μs, suggesting the formation of peroxide intermediate which is a precursor intermediate for evolution of molecular oxygen in the Kok cycle (see Fig. S8). However, peroxide intermediate was not detected by TR-XFEL [116–119], suggesting that its lifetime is short because of a concerted process of second water insertion and release of molecular oxygen in the late stage for oxygen evolution [121]. Thus, our PT-ET mechanism in the text is consisted with the time steps for three events revealed by the TR SFX-XFEL. Therefore, the present PT-ET mechanism for water oxidation is a possible scenario, which is compatible with available XFEL results for the S_3 to S_0 transition through S_4 transition state [116–119].

SVI Multi-copper oxides

SVI.1 Reduction of molecular oxygen into two water molecules in MCO

We have cited three multi-nuclear transition metal complexes in Fig. 1 in the main text. However, the multi-copper oxides (MCO) were not examined in the main text. MCO catalyzes four-electron reduction of molecular oxygen as in the case of C*c*O [3, 4]. Solomon group [5, 6] has extensively investigated the oxygen reduction process on MMO. They have elucidated the mechanism of the reduction of molecular oxygen into two water molecules in MCO illustrated in Fig. 1(c). Here, the oxygen reduction in MCO is examined in relation to that of C*c*O. According to their detailed investigations [5, 6], the fully reduced (FR) state of MCO is given by the four Cu(I) site as shown in eq. (s17), indicating similarity to the R state of C*c*O. Neutral molecular oxygen is inserted at the T2-T3α-T3β-part, providing superoxide anion radical

intermediate (SPI) as illustrated in eq. (s18). The oxygen dianion is formed with one ET in the next stage, namely peroxide intermediate (PI) as shown in eq. (s19),

FR: $Cu(I)_{T1}$-$Cu(I)_{T2}(H2O)$-$Cu(I)_{T3\alpha}Cu(I)_{T3\beta}$ (s17)

SPI: $Cu(I)_{T1}$-$Cu(I)_{T2}(H2O)$-$Cu(I)_{T3\alpha}$-$\bullet^{1-}$O-O-$Cu(II)_{T3\beta}$ (s18)

PI $Cu(I)_{T1}$-$Cu(II)_{T2}(H2O)$-$Cu(I)_{T3\alpha}$-O-O^{2-}-$Cu(II)_{T3\beta}$. (s19)

The next step is the O-O bond fission by the protonation of the oxygen dianion, suggesting the hydroperoxide anion ($^{-}$OOH) intermediate (HPI) in eq. (s20), which has not been observed by the experiments [5, 6]. The proton transfer coupled electron transfer (PT-ET) in Fig. 5 of the main text is supposed to be important from the conversion from PI to HPI. The one ET to HPI provides the native intermediate (NI) in eq. (s21) because of the O-O bond fission, for which participation of the T2 part is essential in a sharp contrast to hemocyanin for oxygen carrier. Proton addition to NI provides the resting intermediate (RS) followed by water release in MCO in eq. (s22). Further PT-ET reactions provide water molecule, which is released to recover the initial fully reduced (FR) state in eq. (s23).

HPI: $Cu(I)_{T1}$-$Cu(II)_{T2}(HO)$-$Cu(II)_{T3\alpha}$-O-OH^{-}-$Cu(II)_{T3\beta}$ (s20)

NI: $Cu(II)_{T1}$-$Cu(II)_{T2}(HO)$-$Cu(II)_{T3\alpha}(O)(OH^{-})Cu(II)_{T3\beta}$ (s21)

RS: $Cu(II)_{T1}$-$Cu(II)_{T2}(HO)$-$Cu(II)_{T3\alpha}(OH^{-})Cu(II)_{T3\beta}$ + H_2O (s22)

FR: $Cu(I)_{T1}$-$Cu(I)_{T2}(H_2O)$-$Cu(I)_{T3\alpha}Cu(I)_{T3\beta}$ + H_2O (s23)

The spectroscopic and computational results for the O-O bond fission in MCO provide significant information for the reverse O-O bond formation for water oxidation in PSII. The NI stage in eq. (s21) corresponds to the P_M state in C*c*O in eq. (18) in the main text and the S_3 state with (4444) and Tyrosine radical [$S_{3abca(R)}$-OH + Tyr161-O•] formed (see Fig. 6(b)) in the third flash in OEC of PSII. Tyr161-O• in C*c*O and PSII is replaced with T1-Cu(II) in MCO, which undergoes oxidation reactions of substrates in MMO [5, 6]. Thus, from the mechanistic interest, Cu-tri-cluster consisted of $Cu(II)_{T2}Cu(II)_{T3\alpha}Cu(II)_{T3\beta}$ has been investigated extensively as described in the review articles [5, 6].

SVI. 2 Spin Hamiltonian models for the tri-copper oxide clusters

Tri-copper triangle in MCO is a typical example of spin frustration system [73, 74] examined in section SIII. EPR and magnetic circular dichroism (MCD) spectroscopies [5, 6] have been extensively performed for MCO. Therefore, spin Hamiltonian model derived in SIII is applicable to investigate spin states of MCO. The Cu-tri-cluster consisted of $Cu(II)_{T2}Cu(II)_{T3\alpha}Cu(II)_{T3\beta}$ is formally regarded as a [3e, 3o] system

investigated by the Hubbard model in Fig. S1 [36]. A spin Hamiltonian model has also been proposed to express the exchange coupling between the Cu(II) ion as shown in eq. (s24a) [5, 6]

$$\boldsymbol{H} = -2J_{12}\,\mathbf{S}_1\bullet\mathbf{S}_2 - 2J_{13}\,\mathbf{S}_1\bullet\mathbf{S}_3 - 2J_{23}\,\mathbf{S}_2\bullet\mathbf{S}_3 \tag{s24a}$$

where J_{ij} denotes the effective exchange integral between $Cu(II)_i$ and $Cu(II)_j$ and $\mathbf{S}_i$ (i = 1–3) is the spin operator for a local spin at the site i. The spin Hamiltonian in eq. (s24a) is re-written a simple form for the equilateral triangle with $J = J_{12} = J_{13} = J_{23}$, providing a spin Hamiltonian as follows [76]:

$$\boldsymbol{H}_{eq} = -J\,[\mathbf{S}_{total}^2 - \mathbf{S}_1^2 - \mathbf{S}_2^2 - \mathbf{S}_3^2], \tag{s25a}$$

where total spin is given by $\mathbf{S}_{total} = \mathbf{S}_1 + \mathbf{S}_2 + \mathbf{S}_3$.

The total low-spin configuration is given by S_{total} = 1/2, providing two different spin alignments; LSI: S_1 = 1/2, S_2 = 1/2 (−1/2), S_3 = −1/2 (1/2) and LSII: S_1 = −1/2, S_2 = 1/2, S_3 = 1/2. On the other hand, total high spin (HS) configuration is given by S_{total} = 3/2 and S_1 = S_2 = S_3 =1/2. Therefore, total energies for these solutions are given by

$$\langle\boldsymbol{H}_{eq}\rangle_{LSI} = -J\,[S_{total}(S_{total}+1) - S_i(S_i+1)\times 3] = -J\,[3/4 - 3/4\times 3] \tag{s26a}$$
$$\langle\boldsymbol{H}_{eq}\rangle_{LSII} = -J\,[S_{total}(S_{total}+1) - S_i(S_i+1)\times 3\,] = -J\,[3/4 - 3/4\times 3] \tag{s26b}$$
$$\langle\boldsymbol{H}_{eq}\rangle_{HS} = -J\,[\,S_{total}(S_{total}+1) - S_i(S_i+1)\times 3] = -J\,[15/4 - 3/4\times 3]. \tag{s26c}$$

Therefore, LSI and LSII are degenerated in energy, indicating the doublet E state. The energy gap between LSI (LSII) and HS states is given by 3J (= −3/4 + 15/4) [76]. In our chemistry notation, J is negative for antiferromagnetic super-exchange interaction. The observed J-value was −105 cm^{-1} for the model complex (tris-OH) [5, 6].

The ab-initio computations have been performed by several computational methods [5, 6]. Both broken-symmetry (BS) and symmetry-adapted (SA) methods are applicable to eq. (s16a) [90]. The CASSCF[27e, 15o]/CASPT2 computation has provided the negative J-value (−35 cm^{-1}), but its magnitude is smaller than the observed value (−105 cm^{-1}). On the other hand, the DD-configuration interaction (CI)-2(1) [3e, 3o] methods have provided the strong negative values, −292 (−239) cm^{-1}. The magnitude of these is larger than the observed value (105 cm^{-1}). Thus, quantitative computation of the J-value for the spin frustration systems such as tris-OH is not so easy.

A spin Hamiltonian model for the equilateral triangle is extended to describe the exchange coupling between the Cu(II) ion for acute ($\delta < 0$) and obtuse ($\delta > 0$) triangles which are rather similar to

MCO as shown in eq. (s24b).

$$\boldsymbol{H} = -2\,(J-\delta)\,\mathbf{S}_1\bullet\mathbf{S}_2 - 2(J-\delta)\,\mathbf{S}_1\bullet\mathbf{S}_3 - 2(J+\delta)\,\mathbf{S}_2\bullet\mathbf{S}_3 \quad \text{(s24b)}$$

$$= -(J-\delta)\,[\mathbf{S}_{\text{total}}^2 - \mathbf{S}_1^2 - \mathbf{S}_2^2 - \mathbf{S}_3^2] - 4\,\delta\,\mathbf{S}_2\bullet\mathbf{S}_3 \quad \text{(s24c)}$$

$$= -(J-\delta)\,[\mathbf{S}_{\text{total}}^2 - \mathbf{S}_1^2 - \mathbf{S}_2^2 - \mathbf{S}_3^2] - 2\,\delta\,[\mathbf{S}_{23}^2 - \mathbf{S}_2^2 - \mathbf{S}_3^2] \quad \text{(s24d)}$$

where T3 Cu exchange-coupled pair [5, 6] is given by $\mathbf{S}_{23} = \mathbf{S}_2 + \mathbf{S}_3$.

The total low-spin configuration for these models is given by $S_{\text{total}} = 1/2$, providing two different spin alignments; LSI: $S_1 = 1/2$, $S_{23} = S_2 + S_3 = 0$ and LSII: $S_1 = -1/2$, $S_{23} = S_2 + S_3 = 1$. On the other hand, total high spin (HS) configuration is given by $S_{\text{total}} = 3/2$ and $S_1 = S_2 = S_3 = 1/2$. Therefore, total energies for these solutions are given by

$$\langle \boldsymbol{H}_{\text{eq}} \rangle_{\text{LSI}} = -(J-\delta)\,[3/4 - 3/4 \times 3] - 2\delta\,[0 - 3/4 \times 2] \quad \text{(s27a)}$$

$$\langle \boldsymbol{H}_{\text{eq}} \rangle_{\text{LSII}} = -(J-\delta)\,[3/4 - 3/4 \times 3] - 2\delta\,[2 - 3/4 \times 2] \quad \text{(s27b)}$$

$$\langle \boldsymbol{H}_{\text{eq}} \rangle_{\text{HS}} = -(J-\delta)\,[15/4 - 3/4 \times 3] - 2\delta\,[2 - 3/4 \times 2]. \quad \text{(s27c)}$$

Therefore, degeneracy between LSI and LSII is removed out in the case of acute and obtuse triangles. The energy gap between LSI and LSII states is given by 4δ, indicating that LSI is more stable than LSII for acute triangle ($\delta < 0$) and the tendency is reversed for obtuse triangle ($\delta > 0$). On the other hand, the energy gap between LSI and HS is $3J + 4\delta$, whereas the energy gap between LSII and HS is given by $3J$.

The ab-initio computations have been also performed for the native intermediate model (NI_C) of MCO [s1, s2]. The CASSCF computation has provided the negative J-value (-11.3 cm^{-1}) and δ-value (-14.2 cm^{-1}), which accord with the acute triangle, but the magnitude of J is too small. The MS-CASPT2 has provided the negative J-value (-59.3 cm^{-1}) and δ-value (-36.2 cm^{-1}). The magnitude of J is still small after PT2 dynamical electron correlation for CASSCF. On the other hand, the DD-configuration interaction (CI)-2 [3e, 3o] method has provided the strong negative J-value; -448 (-433) cm^{-1} and δ-value; -26.5 (-24.8) cm^{-1}, where the corresponding values by MRCI-S are given in parentheses. Thus, quantitative computation of the J-value for the spin frustration systems such as (NI_C) is difficult, indicating the necessity of extended theoretical investigations [s3].

Solomon et al. [5, 6] have determined the effective exchange couplings between the Cu(II) ions by the magnetic circular dichroism (MCD) experiments; $J_{12} = -215$ cm^{-1}, $J_{12} = -235$ cm^{-1} and $J_{23} = -260$ cm^{-1}. The average value of J_{12} and J_{13} for the assumed acute triangle is -225 cm^{-1}. Assuming this average value, we can obtain $J = -242.5$ cm^{-1} and $\delta = -17.5$ cm^{-1}. However, the asymmetry parameter $\delta' = -10$ cm^{-1} is further necessary to reproduce the observed values [5, 6] ; $J_{12} = -225 + 10 = -215$ cm^{-1} and $J_{13} =$

$-225 + 10 = -235$ cm^{-1}. Judging from the experimental *J*-values, the DDCI-2 and MRCI-S methods have overestimated the magnitude of the *J*-value for NI_C. Thus, quantitative computations of the *J*-values are not easy even for the deformed triangles. This may indicate that the MR CC method in Fig. 4 is inevitable for quantitative computations of the energy levels for MCO [5, 6].

[s1] Vancoillie, S., Chalupský, J., Ryde, U., Solomon, E.I., Pierloot, K., Neese, F., & Rulíšek, L. (2010). Multireference ab initio calculations of g tensors for trinuclear copper clusters in multicopper oxidases. *The Journal of Physical Chemistry B*, 114, 7692-7702. https://doi.org/10.1021/jp103098r

[s2] Jones, S.M., & Solomon, E.I. (2015). Electron transfer and reaction mechanism of laccases. *Cellular and Molecular Life Sciences*, 72, 869-883. https://doi.org/10.1007/s00018-014-1826-6

[s3] Vogiatzis, K.D., Polynski, M.V., Kirkland, J.K., Townsend, J., Hashemi, A., Liu, C., & Pidko, E.A. (2019). Computational approach to molecular catalysis by 3d transition metals: challenges and opportunities. *Chemical Reviews*, 119, 2453-2523. https://doi.org/10.1021/acs.chemrev.8b00361